*Proceedings of the Thirty-sixth (2026) International Ocean and Polar Engineering Conference* **www.isope.org**
*Orlando, Florida, USA, May 31-June 5, 2026*

*ISBN 978-1-880653-72-2; ISSN 1098-6189*

# Effects of Bottom Boundary Conditions on Wall-Pressure Fluctuations of a Finite-Span NACA0012 Airfoil

*Yipei Wang[1], Jie Zhu[2], Weiwen Zhao[1], Decheng Wan[1*]*

[1] Computational Marine Hydrodynamics Lab (CMHL), School of Ocean and Civil Engineering, Shanghai Jiao Tong University, Shanghai, China
[2] Wuhan Second Ship Design and Research Institute, Wuhan, China
[*]Corresponding Author

## ABSTRACT

This paper investigates the influence of bottom boundary-condition modelling on wall-pressure fluctuations over a finite-span NACA0012 airfoil using wall-resolved LES. Two configurations, a no-slip wall and a symmetry plane, are compared while keeping all other numerical settings identical. The WRLES setup is validated against available measurements through the mean pressure coefficient *Cp*. The link between horseshoe vortex dynamics and low-frequency pressure amplification near the root is clearly explained and physically consistent.

KEY WORDS: NACA0012; finite-span airfoil; WRLES; wall-pressure fluctuations

## INTRODUCTION

Unsteady surface loading is a pervasive issue in practical flows around engineering structures, with direct implications for structural vibration, fatigue, and aeroacoustics performance. In turbulent flows, wall-pressure fluctuations provide a compact and physically meaningful description of near-wall unsteadiness, reflecting boundary-layer dynamics, separation/reattachment behavior, and shear-layer instabilities. From an aeroacoustics perspective, fluctuating surface pressure is also closely connected to radiated sound through well-established theoretical frameworks and semi-empirical prediction models; accordingly, accurate characterization of pressure-fluctuation intensity and spectral content is a prerequisite for reliable noise assessment and mitigation strategies (Curle and Lighthill 1955; Amiet 1975; Brooks, Pope, and Marcolini 1989, Botero-Bolívar et al. 2023).

Experimentally, measurement capabilities for airfoil surface pressure have advanced substantially in recent years. For the canonical NACA0012 airfoil, high-density measurements have been used to map both the mean pressure distribution and the spatially varying statistics of unsteady surface pressure under a range of inflow and transition-control conditions. These datasets highlight that pressure-fluctuation levels and spectra are strongly non-uniform over the surface and are highly sensitive to the state of the boundary layer and local flow structures, thereby offering stringent benchmarks for numerical simulations beyond mean quantities (Celik et al., 2022).

On the numerical side, the credibility of CFD predictions depends not only on the turbulence modelling and grid resolution, but also on the boundary conditions used to represent surrounding surfaces. This issue is particularly pronounced for configurations involving a nearby wall or ground plane. In simulations of finite wings in ground effect, different ground boundary-condition treatments have been systematically compared, showing that these idealizations can lead to noticeably different aerodynamic outcomes even when the geometry and inflow are unchanged. Moreover, commonly used idealizations such as slip and symmetry may behave similarly for certain mean metrics, whereas a no-slip ground introduces a developing ground boundary layer and can shift the predicted loads (McConkey et al., 2019). These observations suggest that the choice of boundary condition is not merely a numerical detail; it is a modeling decision that can alter near-wall flow organization.

In CFD studies of configurations close to a ground plane, the treatment of the bottom boundary is often a practical modeling choice shaped by both the intended idealization and computational cost, and different treatments (e.g., no-slip versus symmetry/slip) are widely used in practice. More generally, boundary conditions are necessarily idealized representations of the surrounding environment rather than exact replicas of the physical setup. As a result, selecting appropriate boundary conditions is a key part of building credible CFD predictions, and their influence on the quantities of interest should be stated and assessed where possible (Xu et al., 2018). Even when different idealizations produce similar trends in mean pressure, they may diverge in higher-order unsteady metrics, particularly in regions dominated by junction flow.

Despite this progress, most boundary-condition assessments have primarily focused on low-order quantities such as lift/drag coefficients or mean pressure distributions. For problems where root-junction physics is relevant, this can be insufficient: a finite-span airfoil mounted on a bottom boundary typically exhibits strong three-dimensionality near the root, where junction-induced separation may generate coherent structures that can dominate unsteady surface loading and redistribute spectral energy. In this context, it remains unclear to what extent different bottom boundary-condition idealizations—although capable of delivering similar agreement in mean pressure—may diverge in higher-order unsteady metrics, including root-mean-square (RMS) levels and power spectra of wall-pressure fluctuations.

Motivated by this gap, the present study investigates the flow around a finite-span NACA0012 airfoil mounted on a bottom boundary, with the bottom boundary condition treated as the sole modelling variable. Two cases are considered: case I, where the bottom boundary is modelled as a no-slip wall, and case II, where it is modelled as a symmetry plane; all other numerical settings are kept identical. The wall-resolved large-eddy simulation (WRLES) set-up is first validated using the mean pressure coefficient (*Cp*) against available measurements, and the analysis is then extended to vortex-structure evolution and to the RMS and power spectral density (PSD) of wall-pressure fluctuations, with emphasis on the root region. Through this design, the study aims to clarify how the bottom boundary condition influences near-wall three-dimensional flow structures and, consequently, the scale composition and spectral characteristics of wall-pressure fluctuations.

The remainder of this paper is organised as follows. Section 2 describes the numerical methodology, computational domain and mesh, and the validation against experimental mean-pressure data. Section 3 presents the flow-structure evolution and examines root wall-pressure fluctuations in terms of RMS distributions and PSD characteristics. Section 4 summarises the main conclusions and provides guidance on bottom boundary-condition selection for studies targeting unsteady surface pressure statistics.

## NUMERICAL METHODOLOGY AND VALIDATION

### Governing Equations

The present simulations employ wall-resolved large-eddy simulation (WRLES) for an incompressible flow. The governing equations are obtained by applying a spatial filtering operation to the incompressible Navier–Stokes equations. Filtered (resolved-scale) quantities are denoted by a tilde ( %). The filtered continuity equation is

$$\frac{\partial \tilde{u}_i}{\partial x_i} = 0. \tag{1}$$

and the filtered momentum equation is

$$\frac{\partial \tilde{u}_i}{\partial t} + \frac{\partial(\tilde{u}_i\tilde{u}_j)}{\partial x_j} = -\frac{1}{\rho}\frac{\partial \tilde{p}}{\partial x_i} + \nu\frac{\partial^2 \tilde{u}_i}{\partial x_j \partial x_j} - \frac{\partial \tau_{ij}^{\text{sgs}}}{\partial x_j}. \tag{2}$$

Here, $x_i$ is the spatial coordinate in the *i*-th direction, *t* is time, $\tilde{u}_i$ is the *i*-th component of the filtered velocity, $\tilde{p}$ is the filtered pressure, $\rho$ is the fluid density, and $\nu$ is the kinematic viscosity. Repeated indices imply summation. The subgrid-scale (SGS) stress tensor $\tau_{ij}^{\text{sgs}}$ represents the effect of unresolved motions on the resolved field and is defined as

$$\tau_{ij}^{\text{sgs}} = u_i u_j - \tilde{u}_i\tilde{u}_j. \tag{3}$$

The SGS stresses are closed using an eddy-viscosity assumption. The deviatoric part of $\tau_{ij}^{\text{sgs}}$ is modelled as (Nicoud and Ducros)

$$\tau_{ij}^{\text{sgs}} - \frac{1}{3}\tau_{ij}^{\text{sgs}}\delta_{ij} = -2\nu_t \tilde{S}_{ij} \tag{4}$$

where $\delta_{ij}$ is the Kronecker delta, $\nu_t$ is the SGS viscosity, and $\tilde{S}_{ij}$ is the resolved strain-rate tensor,

$$\tilde{S}_{ij} = \frac{1}{2}\left(\frac{\partial \tilde{u}_i}{\partial x_j} + \frac{\partial \tilde{u}_j}{\partial x_i}\right) \tag{5}$$

In this study, the SGS viscosity $\nu_t$ is computed using the WALE (Wall-Adapting Local Eddy-viscosity) model,

$$\nu_t = (C_w\Delta)^2 \frac{\left(S_{ij}^d S_{ij}^d\right)^{3/2}}{\left(\tilde{S}_{ij}\tilde{S}_{ij}\right)^{5/2} + \left(S_{ij}^d S_{ij}^d\right)^{5/4}}. \tag{6}$$

where $C_w$ is the WALE model constant and $\Delta$ is the local filter width. The tensor $S_{ij}^d$ is defined from the filtered velocity-gradient tensor $\tilde{g}_{ij}$ as

$$\tilde{g}_{ij} = \frac{\partial \tilde{u}_i}{\partial x_j} \tag{7}$$

$$S_{ij}^d = \frac{1}{2}\left(\tilde{g}_{ik}\tilde{g}_{kj} + \tilde{g}_{jk}\tilde{g}_{ki}\right) - \frac{1}{3}\delta_{ij}\tilde{g}_{kl}\tilde{g}_{lk} \tag{8}$$

For the unstructured finite-volume mesh employed here, the filter width is taken as

$$\Delta = V^{1/3} \tag{9}$$

where $V$ is the control-volume volume. The isotropic part of the SGS stress, $\frac{1}{3}\tau_{ij}^{\text{sgs}}\delta_{ij}$, is absorbed into the modified pressure and is therefore not treated explicitly.

The governing equations are discretized using the finite-volume method on a collocated mesh. Time integration uses a second-order implicit backward scheme, and spatial derivatives are evaluated using second-order accurate discretization schemes. Pressure–velocity coupling is handled by the PISO algorithm. The momentum equation is solved using PBiCGStab, while the pressure equation is solved using GAMG. The solver tolerance for the velocity equation is set to $10^{-7}$.

### Computational domain and mesh

The geometry is a NACA0012 finite-span airfoil mounted vertically on the bottom boundary. The chord length is, $c = 0.2\text{m}$ and the height is $h = 0.1\text{m}$ . The origin is located at the intersection between the leading edge and the bottom boundary. The *x*-axis points from the leading edge to the trailing edge, the *z*-axis is upward, and the *y*-axis completes a right-handed coordinate system.

The present simulation maintains the same physical conditions as the experiments conducted in Celik et al. (2022). The velocity $u_\infty$ is 20 m/s at the inlet, corresponding to the kinematic viscosity is $\nu = 1.538\times10^{-5}$ m$^2$/s. The corresponding Reynolds number $Re_c = u_\infty c / \nu = 2.60\times10^5$

approximately 40.68 million cells.

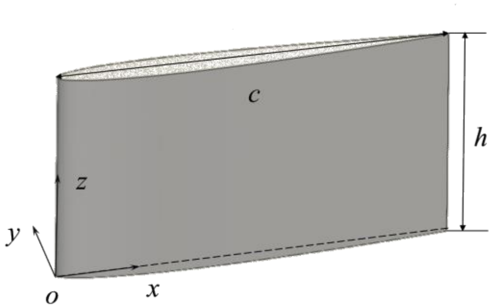


Fig. 1. Geometry of NACA0012 foil.

The computational domain extends $5c$ upstream of the leading edge and $9c$ downstream of the trailing edge. The cross-stream extent is $10c$ , and the spanwise extent is $5c$ , giving an overall size of $15c \times 10c \times 5c$ in the streamwise, cross-stream, and spanwise directions, respectively. A uniform velocity inlet is prescribed at the upstream boundary, while a pressure outlet is applied downstream. The top boundary represents the far-field. All other boundary settings are identical between the two simulations; the only modelling difference is the treatment of the bottom boundary.

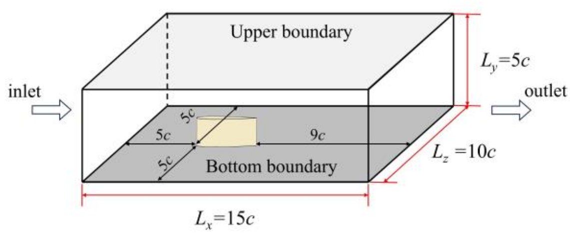


Fig. 2. Computational domain setup.

To streamline later references, the two simulations are defined as follows and are referred to only as case I and case II throughout the remainder of the paper.

Table 1. Summary of simulation cases.

| Case | Bottom Boundary Condition |
|---|---|
| case I | No-slip wall |
| case II | Symmetry plane |

The mesh is generated using snappyHexMesh and is predominantly hexahedral with local refinement. The grid is progressively refined near the airfoil surface, in the near-wake region, and near the bottom boundary. Fig. 3 shows the mesh distribution on the symmetry plane and on a horizontal plane at $z = 0.1$ . The near-wall region is resolved using 35 prism layers with a growth ratio of 1.05. The wall-normal spacing satisfies $\Delta y_w^+ < 1$ , and the streamwise and spanwise spacings satisfy $\Delta x^+ < 30$ and $\Delta z^+ < 12$ , respectively. Our previous study (Fan *et al.*, 2025) qualitatively assessed the effects of $\Delta x^+$ and $\Delta z^+$ on near-wall statistics, particularly the mean velocity profile and wall-pressure fluctuation spectra. The present grid resolution is consistent with these considerations. Additional refinement is applied near the bottom boundary to capture ground-related effects. The final mesh contains approximately 40.68 million cells.

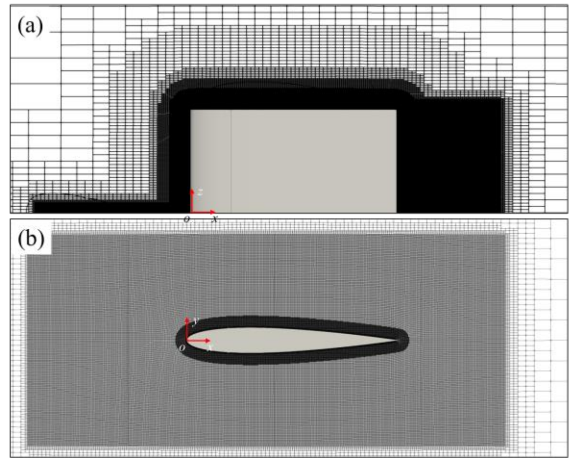


Fig. 3. Computational grid arrangement: (a) side view, (b) top view

To trigger boundary-layer transition and to match the experimental conditions as closely as possible, a square physical trip is placed at $x/c = 0.2$ . Since the experiment does not report the exact trip dimensions, both the trip height and width are set to $0.0023c$. Testing shows that this trip effectively induces transition and improves agreement with the experimental mean-pressure data.

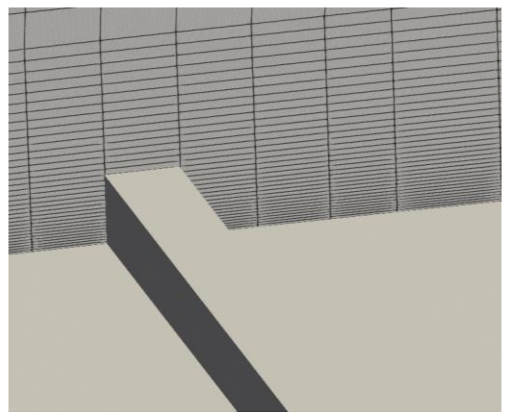

Fig. 4. Configuration of the square trip wire

The time step is set to $\Delta t^+ = 0.005$ , and the maximum Courant number remains below 1.6 throughout the simulations. A total of 13.5 flow-through times is computed. The first 2 flow-through times are used for flow development, and the remaining 11.5 flow-through times are used for statistical sampling and spectral analysis.

**Validation of the present WRLES**

Fig. 5 compares the time-averaged pressure coefficient *Cp* along the airfoil surface with the experimental data. The coefficient *Cp* is a non-dimensional measure of mean surface pressure relative to the free-stream reference. The simulations reproduce the sharp *Cp* drop near the leading edge, the pronounced disturbance around the trip location, and the gradual recovery downstream. Overall, the agreement with the experiment is good (Celik et al. 2022), supporting the credibility of the present setup for subsequent analyses of higher-order unsteady quantities.

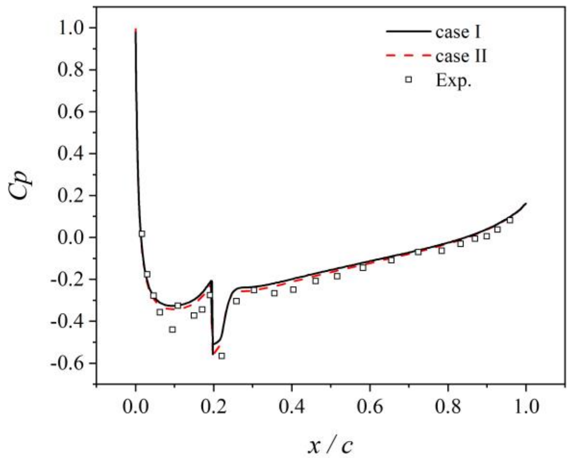


Fig. 5. Comparison of the distributions of the mean pressure coefficient

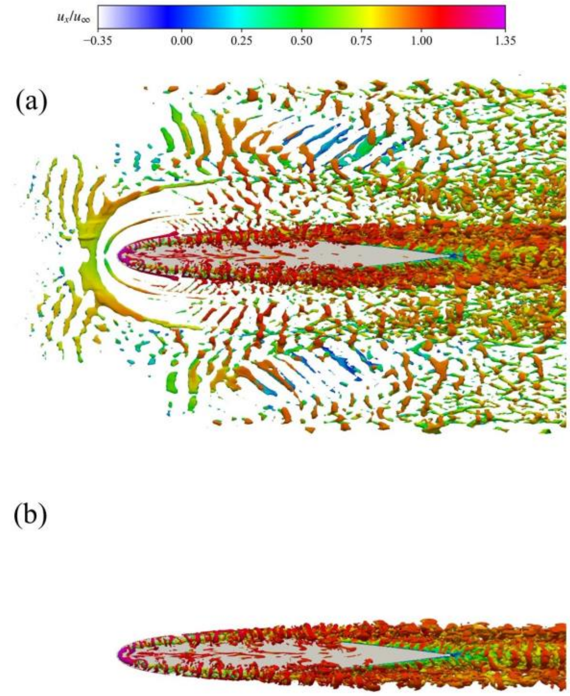


Fig. 7. Top-view comparison of vortex structures near the root and wake: (a) case I; (b) case II.

RESULTS AND DISCUSSION

**Overall analysis of flow-structure evolution**

To characterize the three-dimensional vortex dynamics and the influence of the bottom boundary, vortex structures are identified using a normalized Liutex–Omega method. Iso-surfaces at $\omega_R = 0.52$ are shown for both cases. Figs. 6 and 7 provide three-dimensional and top views, respectively. In each composite figure, (a) case I and (b) case II.

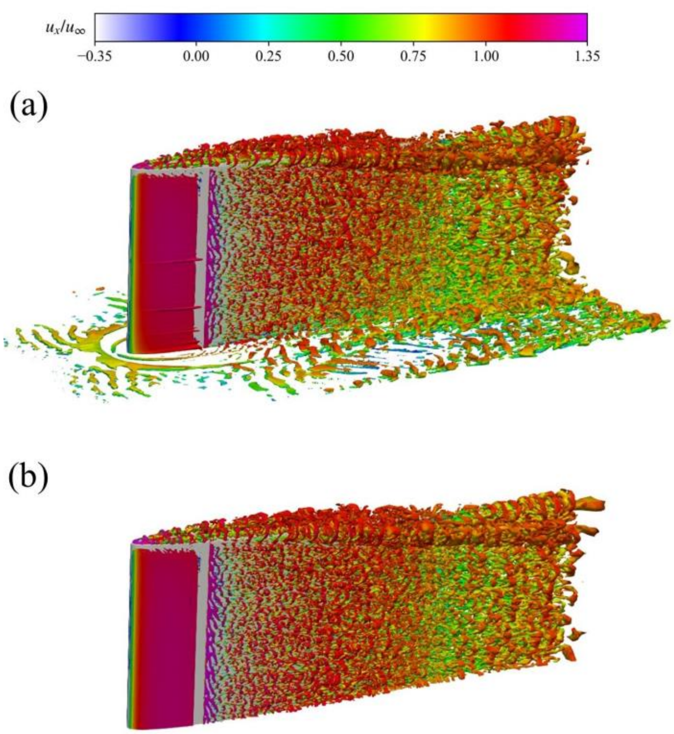


Fig. 6. Three-dimensional vortex structures around the finite-span NACA0012 airfoil: (a) case I; (b) case II.

In case I, the no-slip bottom boundary supports the development of a bottom boundary layer and introduces strong near-wall shear. Combined with the junction geometry, this promotes a distinct three-dimensional separation near the root. The incoming flow is decelerated near the root leading edge and is forced to divert laterally. Together with local separation, this lateral diversion leads to the formation of a horseshoe vortex. The horseshoe vortex extends downstream along both sides of the airfoil and rapidly strengthens the three-dimensionality near the root. As the flow evolves downstream, the horseshoe vortex deforms and breaks up under near-wall shear and three-dimensional disturbances, promoting the formation of a near-wall hairpin-vortex system. In the wake, trailing-edge shedding forms a vortex street with pronounced three-dimensionality, and its spanwise coherence is modulated by upstream junction-related structures.

In case II, the symmetry condition suppresses near-wall shear and bottom boundary-layer development. As a result, the junction-induced blockage–diversion–separation chain is weakened, and a distinct horseshoe vortex does not emerge. The near-wall vortex population at the root is significantly reduced compared with case I. By contrast, in the mid-span and tip regions, both cases still exhibit three-dimensional effects associated with finite-span behavior. Overall, the main differences between the two boundary conditions are concentrated in the root vicinity, which suggests that the most significant differences in wall-pressure fluctuations should also occur near the root.

**Analysis of root wall-pressure fluctuations**

This section quantifies the influence of the bottom boundary condition on wall-pressure fluctuations near the root using RMS and PSD measures. The results are interpreted in the context of the flow structures discussed above.

***RMS distribution of wall-pressure fluctuations***

Fig. 8 compares the RMS distribution of wall-pressure fluctuations for case I and case II. The mid-span and upper regions show only minor differences. In contrast, the root junction region exhibits a clear sensitivity to the bottom boundary condition. In case I, an intensified RMS region appears near the junction, and the bottom surface shows a footprint consistent with junction-related unsteady structures. This aligns with the presence and downstream evolution of the horseshoe vortex and its associated near-wall vortices. In case II, the RMS enhancement near the root is weaker and more spatially confined. This is consistent with the absence of a distinct horseshoe-vortex system.

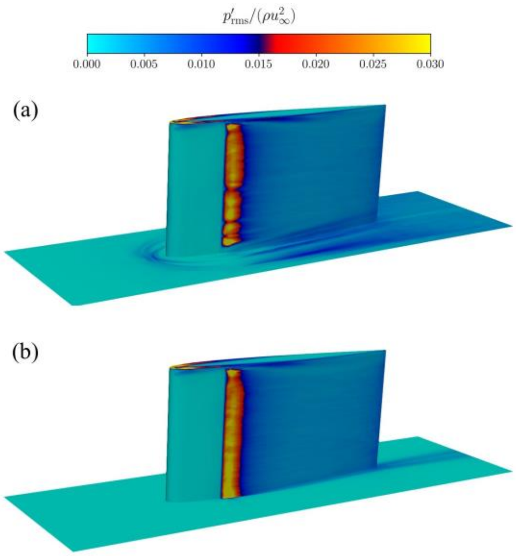


Fig. 8. Comparison of the RMS of wall pressure fluctuations in the bottom region: (a) case I; (b) case II.

***PSD comparison and physical interpretation***

To examine frequency-domain characteristics, three representative wall-pressure probes are selected on the bottom region of the airfoil surface. The probes correspond to upstream, mid-chord, and downstream locations within the root region (P1, P2, and P3). Their positions are shown in Fig. 9. Pressure time histories at these probes are used to compute the PSD.

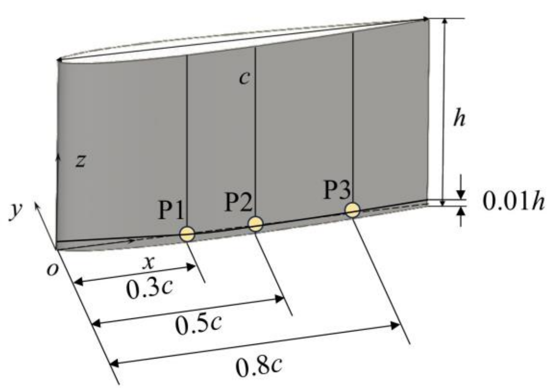


Fig. 9. Locations of typical wall pressure fluctuation measurement points on the bottom surface of the foil

Fig. 10 compares the wall-pressure PSD at the three probes (black solid line: case I; red dashed line: case II; corresponding to Probe 1, Probe 2, and Probe 3). The spectra reveal not only differences in overall levels but also changes in how energy is distributed across frequency bands. This indicates that the bottom boundary condition alters the characteristic scales of unsteady pressure dynamics near the root.

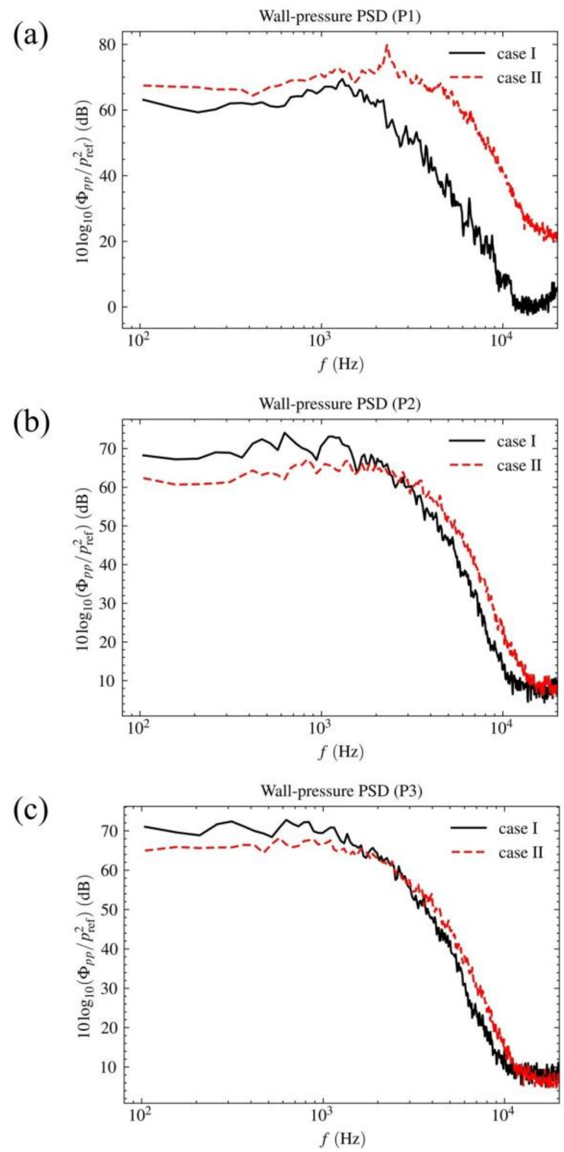


Fig.10. Comparison of the PSD of wall pressure fluctuations at typical root measurement points: (a) P1; (b) P2; (c) P3.

At Probe 1, case II exhibits higher spectral levels across nearly the entire frequency range. The difference is particularly noticeable at mid-to-high frequencies. This suggests that, near the upstream root region, applying a symmetry boundary leads to stronger broadband pressure fluctuations. In case I, the development of a bottom boundary layer and the junction-related three-dimensional structures modify the local near-wall flow and reduce the overall spectral energy at this probe.

Probe 2 shows a clear frequency-dependent behavior. In the low-to-mid frequency range, case I exhibits higher spectral levels than case II. At higher frequencies, case II becomes higher. This pattern is consistent with the scale of junction-related structures. In case I, the horseshoe vortex and the early development of near-wall hairpin vortices represent large-scale three-dimensional unsteadiness. Their relatively slow evolution enhances low-frequency pressure responses. In case II, these large-scale junction structures are weakened, reducing low-frequency energy. Meanwhile, the reduced near-wall shear constraint can favor relatively stronger small-scale disturbances at certain locations, which increases high-frequency spectral levels.

Further downstream, at Probe 3, the spectral differences are smaller overall, but the same tendency remains: case I is slightly higher at low frequencies, whereas case II is higher at mid-to-high frequencies. This reduction in differences is expected because the flow has undergone multiple stages of vortex interaction and breakdown. The local dynamics become closer to a more fully developed three-dimensional turbulent state, which partially mixes and dissipates the initial differences induced at the root. Nevertheless, the persistent trend indicates that the junction-related structures in case I continue to modulate the downstream pressure field.

## CONCLUSIONS

This paper used wall-resolved LES to examine how the bottom boundary condition influences wall-pressure fluctuations over a finite-span NACA0012 airfoil mounted on a bottom surface. Two configurations were investigated: case I, in which the bottom boundary was treated as a no-slip wall, and case II, in which it was represented by a symmetry plane, while all other numerical settings were kept identical. The numerical setup was first assessed by comparing the mean pressure coefficient *Cp* with available measurements, and a good overall agreement was obtained, providing a consistent basis for analyzing higher-order unsteady quantities.

Despite similar performance in the mean-pressure validation, the two cases exhibited markedly different three-dimensional flow structures near the root. case I produced a distinct root horseshoe vortex and its downstream evolution, together with associated near-wall vortex dynamics. In contrast, case II suppressed the development of near-wall shear and bottom-boundary-layer effects at the junction, and a clear horseshoe-vortex system was not reproduced. These structural differences were reflected in the statistics of wall-pressure fluctuations: case I showed a stronger concentration of RMS levels near the root and an enhanced low-frequency contribution in the PSD at representative root probes, consistent with the influence of large-scale, slowly evolving junction structures. case II, by comparison, displayed weaker root-intensity footprints and a redistributed spectral content, with differences diminishing away from the root region.

Overall, the results indicate that agreement in low-order quantities such as mean *Cp* does not guarantee equivalence in higher-order wall-pressure statistics when junction-dominated physics is involved. For studies targeting root unsteadiness, pressure spectra, or noise-relevant metrics, the bottom boundary condition should therefore be selected with care, and a no-slip bottom wall is recommended when reproducing horseshoe-vortex dynamics, and root-driven pressure fluctuations are essential. In regions away from the root, where the flow is less constrained by the junction, the influence of the bottom boundary idealization is comparatively limited.

## ACKNOWLEDGEMENT

This work is supported by the National Natural Science Foundation of China (52131102), to which the authors are most grateful.

## REFERENCES

Amiet, R. K. (1975). "Acoustic Radiation from an Airfoil in a Turbulent Stream, " *J. Sound Vib*, 41(4), 407–420.

Botero-Bolívar, L., dos, Santos, FL., Venner, CH., de, Santana, L. (2023). "Influence of the Freestream Turbulence on Wall-Pressure Fluctuations Along an Airfoil Chord, " *AIAA J*., 61:2309–2313

Brooks, T. F., Pope, D. S., & Marcolini, M. A. (1989). "Airfoil Self-noise and Prediction, " *NASA Reference Publication* 1218.

Celik, A., Bowen, L., and Azarpeyvand, M. (2022). "Experimental Investigation on the Unsteady Surface Pressure Fluctuation Patterns over an Airfoil, " *Phys Fluids*, 34(10), 105134.

Curle, N., and Lighthill, M. J. (1955). "The Influence of Solid Boundaries upon Aerodynamic Sound, " *Proc. R. Soc. London*, *Ser. A*, 231, 505–514.

Fan, G. Q., Chen, H., Zhao, W. W., & Wan, D. C. (2025). "Scaling Laws and Space–time Characteristics of Wall Pressure Fluctuations in an Axisymmetric Boundary Layer with Varying Pressure Gradient, " *J. Fluid Mech*., 1016, A28.

Lighthill, M. J. (1952). "On Sound Generated Aerodynamically I. General Theory, " *Proc. R. Soc. London*, *Ser. A*, 211(1107), 564–587.

McConkey, R., Long, L., Wong, J. G., and Komrakova, A. (2019). "Evaluation of Rans Turbulence Models and Boundary Conditions for CFD Simulations of a Finite Winf in Ground Effect, " *Okanagan Fluid Dynamics Meeting.*

Nicoud, F., and Ducros, F. (1999). "Subgrid-Scale Stress Modelling Based on the Square of the Velocity Gradient Tensor, " *Flow Turbul. Combust*, 62 (3), 183–200.

Xu, P., Liu, X., Zhang, H., Ghista, D., Zhang, D., Shi, C., & Huang, W. (2018). "Assessment of boundary conditions for CFD simulation in human carotid artery, " *Biomech*. *Model. Mechanobiol*., *17*, 1581–1597.